



**HAL**  
open science

# Observed Ocean Surface Winds and Mixed Layer Currents Under Tropical Cyclones: Asymmetric Characteristics

Shengren Fan, Biao Zhang, William Perrie, Alexis Mouche, Guoqiang Liu,  
Huimin Li, Chen Wang, Yijun He

► **To cite this version:**

Shengren Fan, Biao Zhang, William Perrie, Alexis Mouche, Guoqiang Liu, et al.. Observed Ocean Surface Winds and Mixed Layer Currents Under Tropical Cyclones: Asymmetric Characteristics. Journal of Geophysical Research. Oceans, 2022, 127, 10.1029/2021JC017991 . insu-03683303

**HAL Id: insu-03683303**

**<https://insu.hal.science/insu-03683303>**

Submitted on 16 Mar 2023

**HAL** is a multi-disciplinary open access archive for the deposit and dissemination of scientific research documents, whether they are published or not. The documents may come from teaching and research institutions in France or abroad, or from public or private research centers.

L'archive ouverte pluridisciplinaire **HAL**, est destinée au dépôt et à la diffusion de documents scientifiques de niveau recherche, publiés ou non, émanant des établissements d'enseignement et de recherche français ou étrangers, des laboratoires publics ou privés.

Copyright

## Observed Ocean Surface Winds and Mixed Layer Currents Under Tropical Cyclones: Asymmetric Characteristics

Shengren Fan<sup>1</sup>, Biao Zhang<sup>1,2,3</sup> , William Perrie<sup>3</sup> , Alexis Mouche<sup>4</sup> , Guoqiang Liu<sup>3</sup> , Huimin Li<sup>1</sup>, Chen Wang<sup>1</sup>, and Yijun He<sup>1</sup> 

<sup>1</sup>Nanjing University of Information Science and Technology, Nanjing, China, <sup>2</sup>Southern Marine Science and Engineering Guangdong Laboratory (Zhuhai), Zhuhai, China, <sup>3</sup>Fisheries and Oceans Canada, Bedford Institute of Oceanography, Dartmouth, NS, Canada, <sup>4</sup>Laboratoire d'Océanographie Physique et Spatiale, IFREMER, Université Brest, CNRS, IRD, Brest, France

### Key Points:

- Observed near-surface current speeds increase linearly with wind speeds in the four tropical cyclone (TC) quadrants
- Ratios of ageostrophic current speeds to wind speeds are significantly different on left and right sides of TCs
- Satellite and drifting buoy observations show that TC surface winds and currents have asymmetric characteristics

### Correspondence to:

B. Zhang,  
zhangbiao@nuist.edu.cn

### Citation:

Fan, S., Zhang, B., Perrie, W., Mouche, A., Liu, G., Li, H., et al. (2022). Observed ocean surface winds and mixed layer currents under tropical cyclones: Asymmetric characteristics. *Journal of Geophysical Research: Oceans*, 127, e2021JC017991. <https://doi.org/10.1029/2021JC017991>

Received 17 SEP 2021  
Accepted 10 DEC 2021

### Author Contributions:

**Conceptualization:** Biao Zhang  
**Formal analysis:** Biao Zhang, William Perrie, Alexis Mouche, Guoqiang Liu, Huimin Li, Chen Wang  
**Funding acquisition:** Biao Zhang  
**Methodology:** Biao Zhang, William Perrie, Alexis Mouche  
**Supervision:** Biao Zhang  
**Writing – original draft:** Biao Zhang  
**Writing – review & editing:** Biao Zhang, William Perrie, Alexis Mouche, Guoqiang Liu, Huimin Li, Chen Wang

**Abstract** Tropical cyclones (TC) transfer kinetic energy to the upper ocean and thus accelerate the ocean mixed layer (OML) currents. However, the quantitative link between near-surface currents and high wind speeds, under extreme weather conditions, remains poorly understood. In this study, we use multi-mission satellites and drifting-buoy observations to investigate the connections between TC surface winds and currents, including their spatial distribution characteristics. Observed ageostrophic current speeds in the OML increase linearly with wind speeds (for the range 20–50 m/s). The ratios of the ageostrophic current speeds to the wind speeds are found to vary with TC quadrants. In particular, the mean ratio is around 2% in the left-front and left-rear quadrants with relatively small variability, compared to between 2% and 4% in the right-front and right-rear quadrants, with much higher variations. Surface winds and currents both exhibit strong asymmetric features, with the largest wind speeds and currents on the TC right side. In the eyewall region of Hurricane Igor, high winds (e.g., about 47 m/s) induce strong currents (about 2 m/s). The directional rotations of surface winds and currents are resonant and dependent on the location within the storm. Wind directions are approximately aligned with current directions in the right-front quadrant; a difference of about 90° occurs in the left-front and left-rear quadrants. The directional discrepancy between winds and currents in the right-rear quadrant is smaller. Reliable observations of the wind-current relation, including asymmetric features, support published theories developed in idealized numerical experiments to explain the upper ocean response to TCs.

**Plain Language Summary** Observations of surface winds and currents under extreme weather conditions are essential to characterize upper ocean responses to tropical cyclones. To better understand air-sea coupled processes, it is necessary to quantify the connections between surface winds and upper ocean mixed layer currents, and their spatial distribution characteristics. Using an analysis of satellite-derived winds and drifter-observed currents, we find that in severe storm conditions, the near-surface current speeds increase linearly with wind speeds. Moreover, the ratios of ageostrophic current speeds to wind speeds are found to be significantly different on the two different sides of a tropical cyclone track, indicating that the surface winds and currents have strong asymmetry. High-resolution wind fields from spaceborne synthetic aperture radar and currents from collocated drifters further demonstrate the asymmetric features. Stronger winds and currents occur on the right side. Additionally, rotations of surface winds and currents are resonant in the right-front quadrant.

## 1. Introduction

As tropical cyclones (TCs) pass over the ocean surface, the momentum transfer from the atmosphere to the ocean generates strong vertical mixing in the ocean mixed layer (OML) and accelerates the surface currents. While atmosphere and ocean numerical models can be used to simulate TC surface winds and currents (Glenn et al., 2016; Seroka et al., 2017), the accuracy of such modeling is restricted by several factors, such as uncertainty in the initial conditions, surface forcing, parameterization schemes etc. Thus, observations of surface winds and currents are essential to develop and test understanding of the responses of the upper ocean to TCs. From the perspective of observations, buoys, moorings, dropsondes and aircraft reconnaissance are capable of measuring surface winds and currents in TCs (D'Asaro et al., 2014; Zhang et al., 2016), but these meteorological and oceanographic observations are still relatively rare. Wave gliders can simultaneously observe surface winds and currents in the TC cores (Mitarai & McWilliams, 2016), but only provide measurements along the glider tracks.

To better understand the upper ocean response and feedback to TCs, intensive wind and current observations under extreme weather conditions are extremely desirable.

Satellite scatterometers and synthetic aperture radars (SARs) provide high-quality ocean surface wind measurements, even for severe storm-forced winds. Advanced scatterometer (ASCAT) wind vectors around TCs have been evaluated, using collocated GPS dropsonde wind observations, and found to show a bias of  $-1.7$  m/s and a root-mean-square error (RMSE) of  $5.3$  m/s, for wind speeds up to  $50$  m/s (Chou et al., 2013). ASCAT data have been used to elucidate details of the wind variability in extratropical cyclones and polar lows (Schyberg et al., 2015; Zabolotskikh et al., 2014). Compared to the scatterometer, SAR has much higher spatial resolution and can therefore capture the fine-scale features of the wind field. High-resolution TC surface wind fields can be derived from cross- or dual-polarization SAR measurements (Fan et al., 2020; Mouche et al., 2017; Zhang and Perrie, 2012; Zhang et al., 2014). The accuracy of SAR-retrieved TC wind fields has been systematically evaluated using collocated airborne stepped frequency microwave radiometer (SFMR) data, dropsondes, QuikSCAT and WindSat wind observations. The RMSE of SAR-derived winds is about  $5$  m/s, for wind speeds up to  $75$  m/s (Mouche et al., 2019). Ocean surface wind fields from SARs and scatterometers have been widely used to analyze the characteristics of TC structure (Chavas & Emanuel, 2010; Zhang et al., 2020, 2021).

Spaceborne L-band radiometers, onboard the Soil Moisture Active/Passive (SMAP) or the Soil Moisture and Ocean Salinity (SMOS) satellites, are excellent passive microwave sensors to measure TC wind speeds. This is due to the fact that L-band wind-induced ocean surface brightness temperatures are sensitive to high wind speeds and much less susceptible to rain attenuation than higher frequency Ku-band scatterometers or C-band SARs (Meissner et al., 2017; Reul et al., 2012; Yueh et al., 2016). A comparison between maximum wind speeds derived from SMOS and best-track data yields a RMSE of  $7.5$  m/s for wind speeds up to  $60$  m/s (Reul et al., 2016). Statistical comparisons between SMAP-derived TC surface wind speeds and SFMR along-track measurements, have shown that a standard deviation of wind speed of  $3.11$  m/s for wind speeds between  $10$  and  $70$  m/s (Meissner et al., 2017). Compared with the best-track reports, the RMSE of SMAP-derived maximum TC wind speed is  $5.8$  m/s, for the wind speeds in the range of  $17\sim 80$  m/s (Zhang et al., 2021). Moreover, a previous study has demonstrated that the combination of L- and C-band satellite radiometer observations has capability to provide valuable information about the TC surface wind structure (Reul et al., 2017).

The ratio of surface current speed to wind speed, namely the surface drift ratio, is of central importance to SAR remote sensing of ocean surface currents under extreme weather conditions, because storm-induced strong surface currents lead to large Doppler shift. Moreover, it is essential to investigate the spatial patterns of surface winds and currents in storms in order to provide better understanding of oceanic responses to winds in the storm core. Studies have shown that hurricane-induced surface currents on the left side of track are expected to be considerably smaller than those on the right side because the rotation of wind stress is counterclockwise on the left side, which is unfavorable for generating resonance between wind stress and the wind-driven inertial current (Price, 1981; Sanford et al., 2011). The left-right asymmetry in hurricane surface currents may also be related to Langmuir turbulence (Sullivan et al., 2012). Under low to moderate winds, the surface drift ratio has been reported to vary in the range of  $1.5\%–4.1\%$ , according to laboratory experiments and field observations (Brown, 1991; McNally, 1981; Peterson, 1985; Wu, 1968), or  $2\%–3\%$  from coastal high-frequency radar measurements (Shay et al., 2007). Based on QuikSCAT high wind speed observations, a previous study showed that the estimated near-surface mean drift ratio was about  $2\%$  (Chang et al., 2012). However, the quantitative connection between strong surface currents and high wind speeds under TC conditions is still poorly resolved, and it is therefore not clear whether surface drift ratios from existing studies are robust. Synergistic measurements of ocean surface winds and currents from multi-mission satellites and drifters under extreme weather conditions provide an unprecedented opportunity to ascertain the connections between TC surface winds and currents, including their spatial distribution characteristics.

In this paper, for the first time, we explore the link between surface winds and currents, and reveal their asymmetric features in TCs, using the wind fields as derived from SAR, scatterometer, radiometer observations, and current measurements from drifters. We show that observed near-surface current speeds increase linearly with wind speeds in the four TC quadrants under high wind conditions ( $20–50$  m/s). Moreover, the ratios of ageostrophic current speeds to wind speeds are significantly different on left and right sides of TC. These two important findings are found to be consistent, when analyzed with four different satellites, whether for C-band SAR and scatterometer, or L-band radiometers. Based on analysis of case studies and statistical analysis of a larger data set,

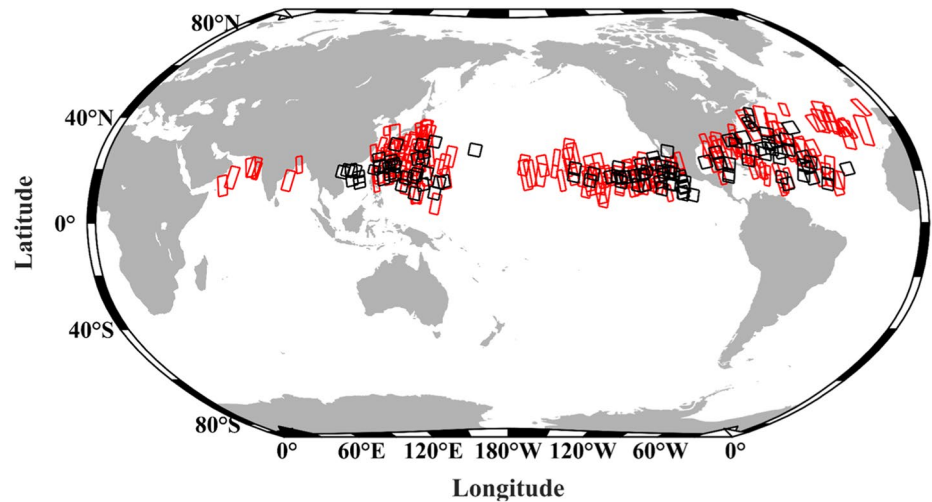


**Figure 1.** The geographic locations of synthetic aperture radars images of 170 TCs. The red and black squares denote S1-A/B and RS-2, respectively.

including satellite and drifting buoy observations, we are able to clearly reveal the asymmetric characteristics of TC surface winds and currents. In Section 2, the datasets are described. Section 3 presents the method and results. A summary is given in Section 4.

## 2. Datasets

In this study, SAR, ASCAT, SMOS, and SMAP observed winds and drifter-measured currents in TCs, are used to investigate the connection between surface wind and near-surface current and their asymmetric features.

### 2.1. SAR and ASCAT Wind Data

A total of 170 TCs were observed by C-band Sentinel-1A/B (S1-A/B) and RADARSAT-2 (RS-2) SAR over the North Atlantic (NA), Northeast Pacific (NEP), Northwest Pacific (NWP), and Indian Ocean (IO) between July 2008 and September 2020. The geographic locations of the TC SAR images are shown in Figure 1. The imaging modes employed for these observations were interferometric wide (IW) and extended wide (EW) for S1-A/B and ScanSAR wide for RS-2. The swath widths for the IW and EW modes are 250 and 400 km, respectively; for the ScanSAR wide mode, the swath width is 500 km. The incidence angles range from 17° to 49°, depending on the sensor and/or mode. For S1-A/B, the spatial resolutions in the range and azimuth directions for the IW and EW modes are 5 × 20 m and 20 × 40 m, respectively; for the RS-2 ScanSAR wide mode, the resolution is 73–163 × 78–106 m. In this study, we use established retrieval algorithms for SAR TC wind speeds and wind directions (Fan et al., 2020; Mouche et al., 2017) and dual-polarization (VV + VH) SAR images, to derive wind fields with a 3-km resolution. Additionally, ASCAT surface wind fields from 296 TCs were obtained over the NA, NEP, NWP, and IO for the period from March 2007 to May 2020. ASCAT is the advanced C-band scatterometer onboard the series of meteorological operational (MetOp) satellites. It consists of two sets of three antennas, which enable simultaneous observations from three directions in each of its two wide swath configurations (Figa-Saldaña et al., 2002). The primary objective of ASCAT is to measure global ocean surface wind fields for use in weather forecasting and climate research. ASCAT daily gridded wind data, with a spatial resolution of 0.25° × 0.25°, were obtained from the Remote Sensing Systems website (<http://www.remss.com/missions/ascat/>).

### 2.2. SMAP and SMOS Wind Data

Compared to active microwave sensors such as SAR (S1-A/B or RS-2) and scatterometer (ASCAT), passive radiometers have larger coverage and lower resolution. For the radiometer onboard SMAP, the spatial resolution and the coverage are about 40 and 1,000 km, respectively. In this study, SMAP L-band radiometer-measured surface wind fields from 335 TCs were acquired over the NA, NEP, NWP, and IO between April 2015 and December

2020. SMAP wind data with a spatial resolution of  $0.25^\circ \times 0.25^\circ$  are freely available from the Remote Sensing Systems website ([www.remss.com/missions/smap/](http://www.remss.com/missions/smap/)). The SMAP radiometer has the ability to provide accurate estimates of TC intensity ( $\sim 70$  m/s) even in heavy rainfall conditions (Meissner et al., 2017). In addition to SMAP, we also collected wind data from 356 TCs observed by the L-band radiometer onboard the SMOS satellite between May 2010 and September 2015 over the NA, NEP, NWP, and IO. The swath width of the SMOS radiometer is 1,200 km and the spatial resolution varies within the swath, from  $\sim 30$  to  $\sim 80$  km. SMOS gridded wind products with a spatial resolution of  $0.25^\circ \times 0.25^\circ$  are publicly available at [www.smosstorm.org](http://www.smosstorm.org).

### 2.3. Drifter Current Data

The Global Drifter Program (GDP) maintains about 1,300 satellite-tracked surface drifting buoys that provide in situ observations of current velocities in the OML, as well as measurements of the sea surface temperature, atmospheric pressure, sea surface salinity, and wind. Direct measurements of current velocities in the OML were obtained from drifters at a nominal depth of 15 m (Lumpkin et al., 2013). Based on the 6-hourly drifter observations and best-track data, previous studies have shown current speeds over 2 m/s under category-4 and -5 TCs, with the strongest mean currents to the right side of the storm track (Chang et al., 2013). A data set of global surface drifter currents at hourly resolution were derived by Elipot et al. (2016), which are freely available at [https://www.aoml.noaa.gov/phod/gdp/hourly\\_data.php](https://www.aoml.noaa.gov/phod/gdp/hourly_data.php). Compared to standard 6-hourly drifter current products, this high temporal resolution data set is a new valuable tool that can be used to study near-surface currents under TC conditions.

## 3. Method and Results

### 3.1. Observed Near-Surface Currents and Drift Ratios in TCs

High wind speeds (20–50 m/s) observed by multi-mission satellites such as SAR, ASCAT, SMAP, and SMOS, together with collocated current data from GDP drifters, obtained from 2007 to 2020, were analyzed in order to determine the relationships between the observed current speeds and wind speeds, as well as the near-surface drift ratios in the four geographic TC quadrants. For collocation, we only selected those drifters within satellite coverage. Collocated satellite and drifter data were required to fall within a time window of 2 hr, which produced a total of 319 and 889 match-up pairs for SAR and ASCAT, 922 and 990 for SMAP and SMOS, respectively. Drifter-measured currents in the OML consist of geostrophic current, ageostrophic current and Stokes drift; the surface geostrophic current can be estimated from the altimeter sea surface height data. To obtain the ageostrophic current, we subtracted the geostrophic current and Stokes drift from the drifter current. Daily sea surface height data are freely available from AVISO website (<https://www.aviso.altimetry.fr/en/data/products/sea-surface-height-products.html>). The Stokes drift can be estimated from realistic wave spectra (Ardhuin et al., 2009). In our study, however, no buoy-measured directional wave spectra were collocated with satellite winds and drifter currents. Here, we first use an empirical equation (Clarke & Van Gorder, 2018) to estimate surface Stokes drift, which is given as follows

$$U_{\text{Stokes}} = 4.4u_* \ln(0.0074U_{10}/u_*) \quad (1)$$

where,  $U_{10}$  is the wind speed at 10-m height and  $u_* = \sqrt{\tau/\rho_w}$  is the friction wind speed.  $\rho_w$  is the water density,  $\tau = \rho_{\text{air}} C_d U_{10}^2$  is the wind stress,  $\rho_{\text{air}}$  is the air density, and  $C_d = 10^{-5}(-0.160U_{10}^2 + 9.67U_{10} + 80.58)$  is the drag coefficient for high wind speeds ( $U_{10} \leq 50$  m/s) (Hwang, 2011). In this study,  $\rho_w$  and  $\rho_{\text{air}}$  are set to constants of 1,030 kg/m<sup>3</sup> and 1.15 kg/m<sup>3</sup>, respectively. Subsequently, the Stokes drift at any given depth may be estimated following (McWilliams & Restrepo, 1999),

$$U^s(z) = U_{\text{Stokes}} \exp \left[ -\frac{4\sqrt{g|z|}}{W} \right] \quad (2)$$

where,  $W = U_{10}$ ,  $g$  is the acceleration of gravity,  $z$  is the water depth. Previous studies have reported that the hurricane-induced surface Stokes drift can account for up to 20% of the surface current speed (Curcic et al., 2016). Stokes drift at 15-m depth is much smaller than that at the ocean surface, because it rapidly decays with depth,

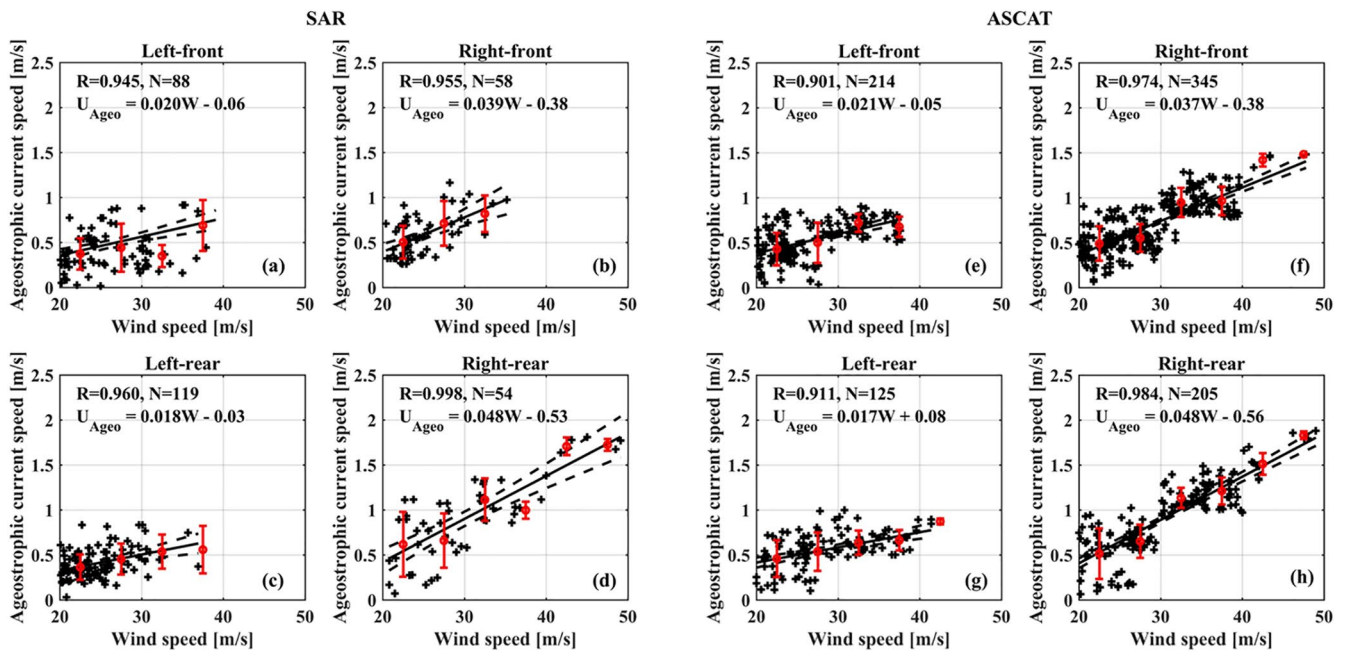


**Figure 2.** Dependence of the ageostrophic current speeds on the surface wind speeds in the four tropical cyclone quadrants. (a)–(d) and (e)–(h) were derived using synthetic aperture radars and Advanced scatterometer data, respectively. Red circles and error bars represent the mean values and standard deviations of ageostrophic current speed (wind speed bin is 5 m/s). Linear regression lines (solid black) are also shown.

according to Equation 2. For example, under TC conditions, the estimated Stokes drift at 15-m depth is 0.13 m/s for a wind speed of 40 m/s, which is very close to that calculated from simulated surface wave spectra (Liu et al., 2021).

Figure 2 presents the dependency of the ageostrophic current speeds on SAR and ASCAT wind speeds in the four TC quadrants. The observed ageostrophic current speeds are found to increase linearly with increasing wind speeds (20–50 m/s). According to Kudryavtsev et al. (2019), the OML thickness for a fast-moving TC is approximately proportional to,

$$h \sim U_{10} [R_{\max} / (N U_h)]^{1/2} \quad (3)$$

where,  $N$  is the Brunt-Väisälä frequency for the seasonal pycnocline,  $U_{10}$  is ocean surface wind speed at 10-m height,  $R_{\max}$  is the radius of maximum wind, and  $U_h$  is the TC's translation speed. The wind-driven current speed in the OML for a moving TC (Price, 1983) can be approximately expressed as

$$U_s \sim \tau R_{\max} / (h U_h) \quad (4)$$

where,  $\tau$  is wind stress ( $\tau = \rho_{\text{air}} C_d U_{10}^2$ ) which can be estimated from air density ( $\rho_{\text{air}}$ ), drag coefficient ( $C_d$ ) and  $U_{10}$ . Substituting Equation 3 into Equation 4 gives the result for  $U_s$ ,

$$U_s \sim \left( \frac{\tau}{U_{10}} \right) (N R_{\max} / U_h)^{1/2} \quad (5)$$

By inserting the formula of wind stress into Equation 5,  $U_s$  can be represented as

$$U_s \sim U_{10} (N R_{\max} / U_h)^{1/2} \quad (6)$$

Thus, ageostrophic OML current speeds are proportional to wind speeds. Moreover, in Figure 2, we also find that the ageostrophic current speeds in the right-front and right-rear quadrants are greater than those in the left-front and left-rear quadrants. These trends are further confirmed by SMAP and SMOS data, which are clearly illustrated in Figure 3. In the northern hemisphere, on the right side of the TC track, wind stress is resonant with near-inertial currents because they have very close frequencies and directions. However, conditions are not

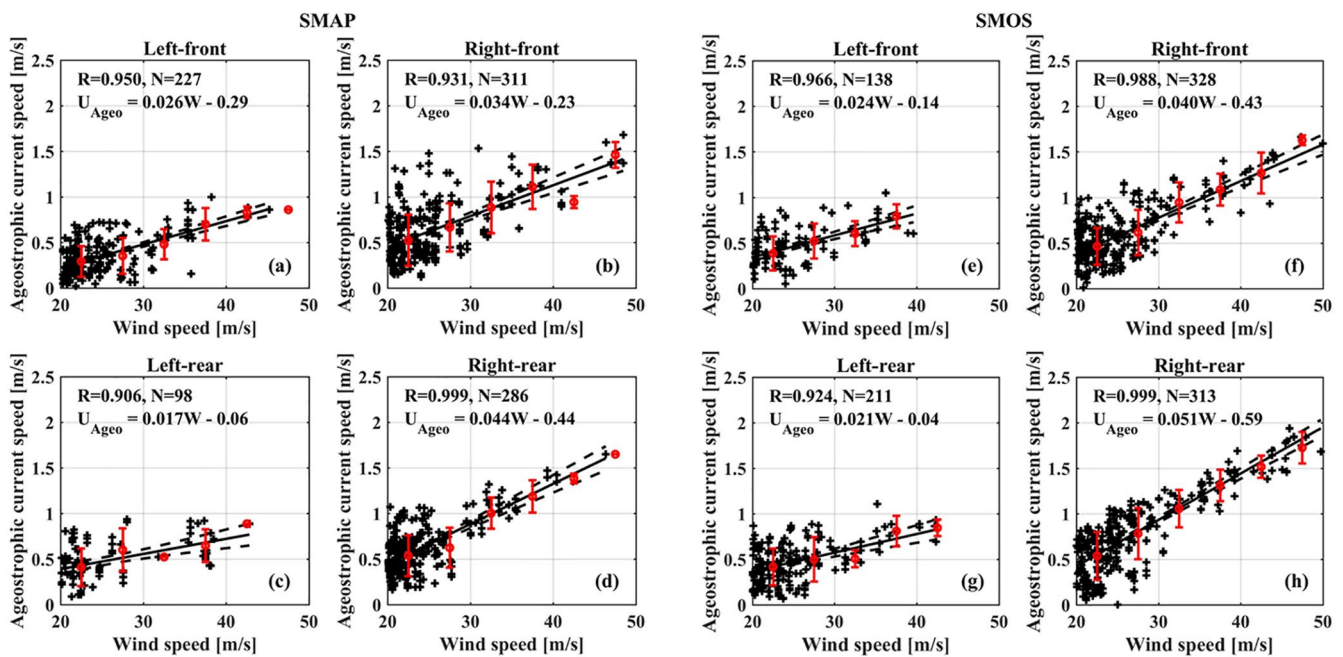


**Figure 3.** Dependence of the ageostrophic current speeds on the surface wind speeds in the four tropical cyclone quadrants. (a)–(d) and (e)–(h) were derived using Soil Moisture Active/Passive and Soil Moisture and Ocean Salinity data, respectively. Red circles and error bars represent the mean values standard deviations of ageostrophic current speed (wind speed bin is 5 m/s). Linear regression lines (solid black) are also shown.

favorable on the TC left side due to opposite directions of these variables; thus, the resonance on the right side results in stronger OML currents than on the left side (Price, 1981). Moreover, on the left side, the winds are moving in an opposite direction to the TC's forward movement, leading to relatively weaker winds and thus less input of momentum fluxes than those on the right side. This is another possible reason for the left-right asymmetry in currents. This characteristic is also exhibited in the estimated near-surface drift ratio,  $\gamma_{ageo}$  (ratio of the ageostrophic current speed to the wind speed). As shown in Figures 4 and 5, whether for SAR and ASCAT, or SMAP and SMOS, the mean value of  $\gamma_{ageo}$  is around 2% in the left-front and left-rear quadrants, which is consistent with previous results from QuikSCAT observations (Chang et al., 2012). By comparison, the ratio in the right-front and right-rear quadrants ranges between 2% and 4%; which are larger than those on the left side. We also use collocated SAR, ASCAT, SMOS and SMAP wind speeds, drifter currents, and translation speed from best-track data to examine the relation between observed drift ratio and the dimensionless parameter in Equation 6. Results did not show any dependence of the observed drift ratio on the combination of TC parameters ( $R_{max}$  and  $U_h$ ) and the ocean stratification ( $N$ ), whether for the right side or the left side of the TC's track.

To examine the coupling of surface winds and currents in TCs, we estimate the near-surface drift angle (relative angle between the current and the wind) using collocated SAR wind data and drifter current measurements. A recent statistical comparison between SAR-retrieved TC wind directions and those measured by buoy, dropsonde, radiometer, and scatterometer has shown that the RMSE of wind directions is 13.3° (Fan et al., 2020). Accordingly, it is reasonable to use SAR-derived wind directions and drifter-measured current directions to estimate the surface drift angle, when no in situ wind directions are available under TC conditions. Figures 6a–6d show that, in the TC right-front and right-rear quadrants, 78% of the drift angles are in the range of 0°–60°, and in the left-front and left-rear quadrants, 57% are between 60° and 120°. On the right side of the TCs, 36% of the drift angles are smaller than 30°. As illustrated in Figures 6e–6h, similar results are also obtained for ASCAT but with more directional variability. These results indicate that on the TC right side, the wind-driven inertial current is much stronger and dominates the total current field, thus leading to a smaller drift angle (wind-flow misalignment). On the TC left side, however, the inertial current is weaker due to weak resonance; therefore, its contribution to the total current field is smaller than that on the right side, resulting in a relatively larger drift angle. A previous study has shown that the RMSE of SMAP wind direction is 18.4° for wind speeds in the range of 12–30 m/s,

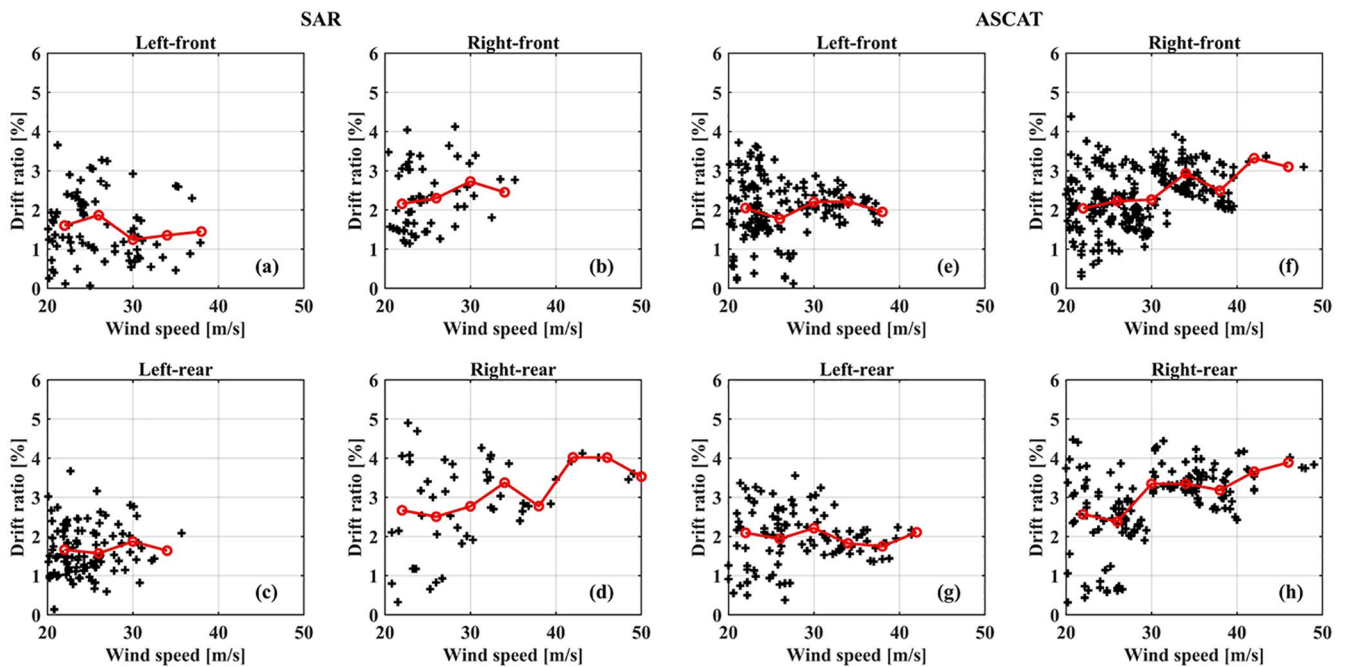


**Figure 4.** Dependence of the near-surface drift ratios on surface wind speeds in the four tropical cyclone quadrants. (a)–(d) and (e)–(h) were derived using synthetic aperture radars and Advanced scatterometer data, respectively. Red lines represent the mean drift ratios.

indicating that the SMAP radiometer can provide reasonable wind directions for tropical depression and tropical storm intensities (Yueh et al., 2016). However, the SMAP wind direction error might become larger when wind speeds exceed the hurricane-force threshold. In addition, SMOS and SMAP storm products do not provide wind direction. Thus, SMAP and SMOS TC wind directions cannot be used to calculate the surface drift angles.

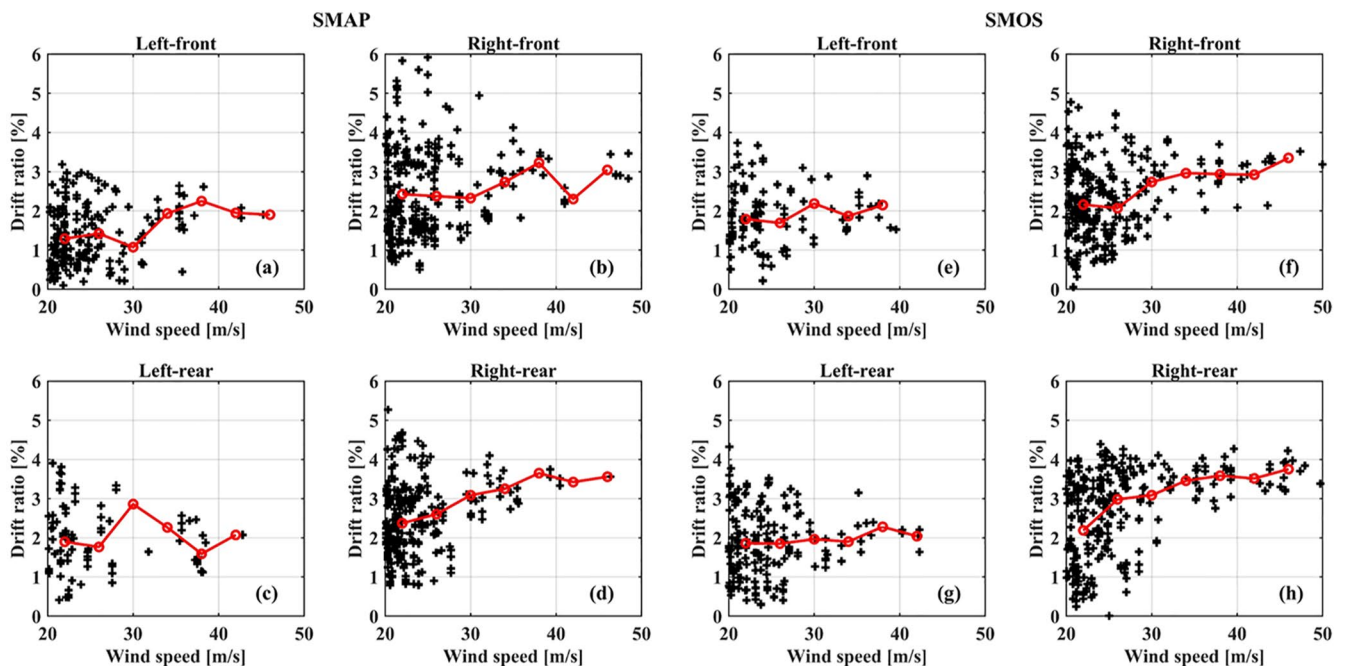


**Figure 5.** Dependence of the near-surface drift ratios on surface wind speeds in the four tropical cyclone quadrants. (a)–(d) and (e)–(h) were derived using Soil Moisture Active/Passive and Soil Moisture and Ocean Salinity data, respectively. Red lines represent the mean drift ratios.

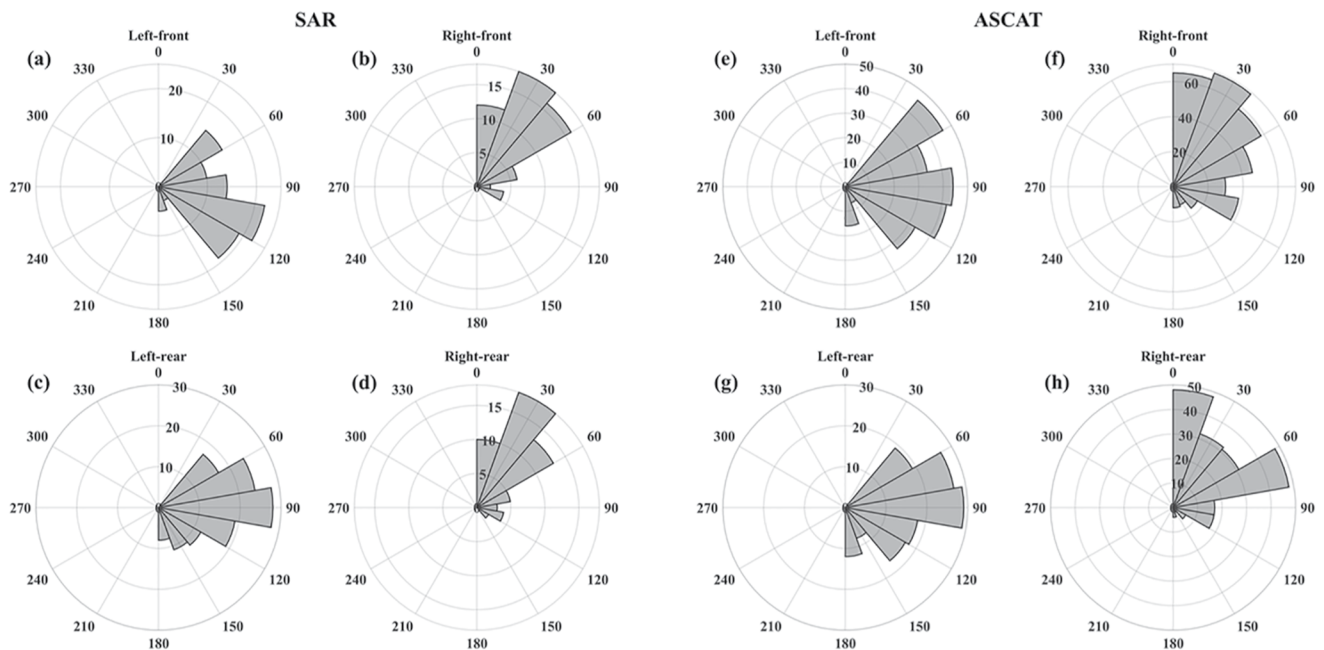


**Figure 6.** Absolute value of the differences in directions between the ageostrophic currents and surface winds in the four tropical cyclone quadrants. (a)–(d) and (e)–(h) were derived using synthetic aperture radars and Advanced scatterometer data, respectively.

### 3.2. Asymmetry in Observed TCs Surface Winds and Currents

In Section 3.1, the relationship between surface winds and OML currents under TC conditions was examined statistically, based on SAR, ASCAT, SMAP, and SMOS observations. In this section, we further assess the asymmetry of winds and currents in TCs. Tropical storm Kalmaegi became a typhoon on 14 September 2014 and passed over a cross-shaped observational array in the South China Sea, late on September 15. As shown in Figure 7a, two stations (B2 and B4) of this array were located on the left and right sides of Kalmaegi's track, respectively, both within the radius of maximum winds. The shortest distances from B2 and B4 to the track are 35 and 118 km, respectively, as estimated using the Joint Typhoon Warning Center best track data set. Surface winds and currents were measured by the weather stations and ADCPs at B2 and B4. At stations B2 and B4, ocean currents were measured using two downward-looking ADCPs, which have operating frequencies of 150 and 300 kHz. The sampling intervals for currents were 8 and 4 m, respectively. In our study, ADCP-measured currents at 14 and 16 m beneath the ocean surface were used because these two depths are comparable to the nominal depth of 15 m used for the current observations made by GDP drifters. The wind speeds were measured by a weather station (AIRMAR-200WX) located at 4 m above the sea surface; these data were adjusted to 10 m above sea level using a logarithmic wind profile equation provided by Edson et al. (2013). Details regarding the observational array and associated measurements of winds and currents are described by Zhang et al. (2016).

Figures 7b–7c show hourly time series of averaged wind speeds and current speeds at stations B2 and B4. Before the arrival of Kalmaegi, the wind and current speeds gradually increased at the two stations until 13:00 UTC on September 15. Kalmaegi moved over B4 earlier than B2, and hence the surface wind at B4 reached its maximum prior to that at B2, as shown in Figure 7b. Although station B2 is on the left side of the track, it is much closer to the track than B4; the maximum wind speed at B2 exceeds that at B4, with Kalmaegi almost passing over B2. Figure 7c illustrates that the OML current speeds at B4 (0.39~1.16 m/s) on the right side tend to be stronger than those at B2 (0.23~0.56 m/s) on the left side, for the period 07:00–20:00 UTC on September 15. Specifically, wind speeds at B2 and B4 are almost same (25 m/s) at 15:00 UTC on September 15, while the current speed at B4 (1.16 m/s) is significantly larger than that at B2 (0.53 m/s). These results agree well with statistics shown in Section 3.1. After the passage of Typhoon Kalmaegi, B4 experienced lower wind speeds than B2 because the former is much farther away from the storm center. Moreover, as presented in Figures 7d–7e, significant directional differences exist between winds and currents at B2, indicating that winds and currents are not obviously resonant

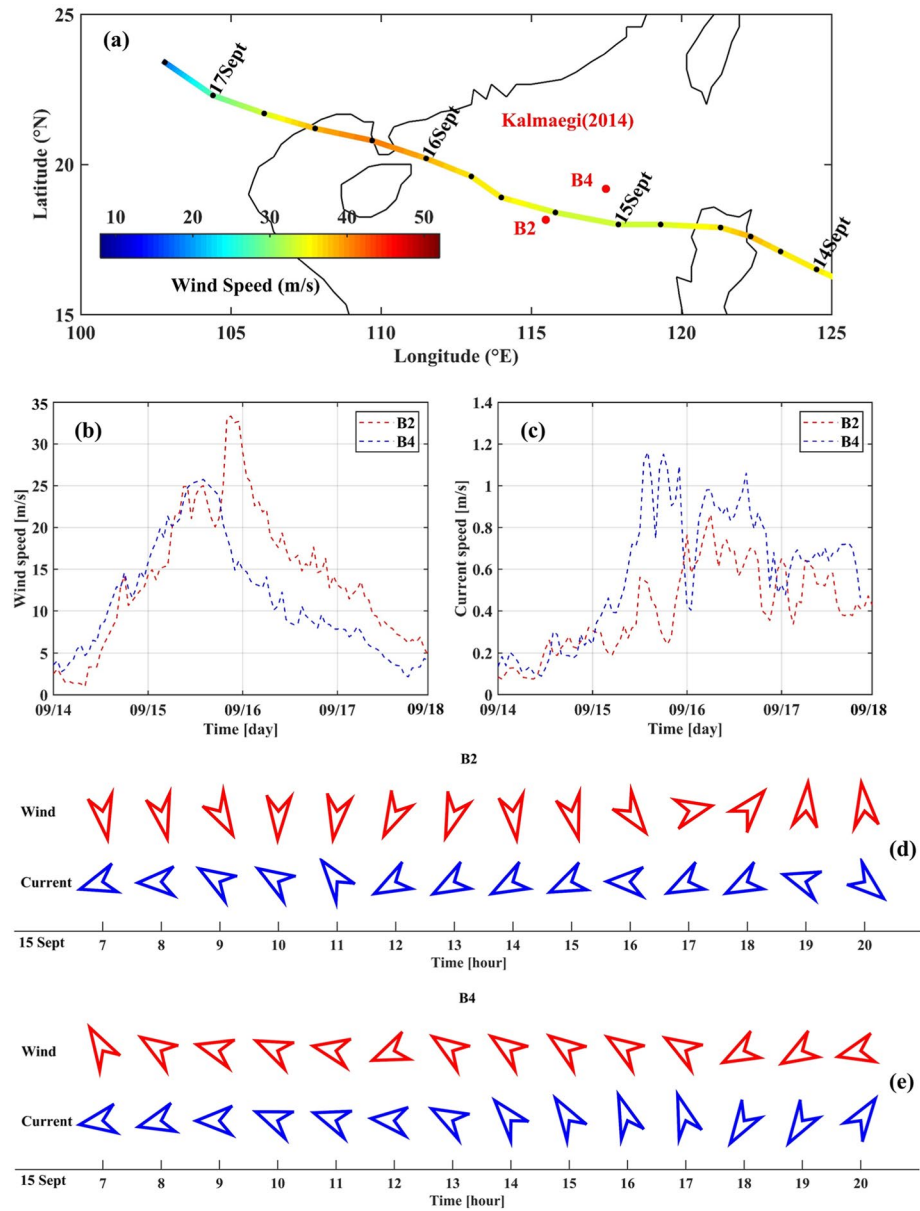


**Figure 7.** (a) Best track for Typhoon Kalmaegi (2014) from the Joint Typhoon Warning Center. Buoy positions are marked by red dots (B2 and B4). The color bar shows maximum sustained wind speed (m/s), which indicates typhoon intensity. (b)–(c) Time series of observations of surface wind speeds and current speeds measured at stations B2 and B4. (d)–(e) Hourly averaged wind and current directions at B2 and B4 during the period between 07:00 and 20:00 UTC on September 15.

on the left side of the track. Compared to B2 on the storm's left side, the directional differences at B4 are much smaller on the right side.

To further illustrate the asymmetry of winds and currents under TC conditions, we selected two cases where drifters are inside the SAR footprint. Figures 8a–8b show high-resolution wind fields from Hurricanes Bertha and Igor derived from RS-2 dual-polarization SAR images obtained at 10:14 UTC on 12 July 2008, and 10:11 UTC on 19 September 2010, respectively. The asymmetry in the SAR-derived high-resolution winds is quite clear, with the maximum wind speed occurring on the right side of the track. In addition to observations of surface winds, a total of 7 drifters were located in the four quadrants of Hurricanes Bertha and Igor and provided near-surface current measurements. For Hurricane Bertha, the drifter-measured current speeds in the right-rear quadrant (0.46–0.53 m/s) are higher than those in the left-front (0.25–0.33 m/s) or left-rear quadrants (0.18–0.28 m/s). In

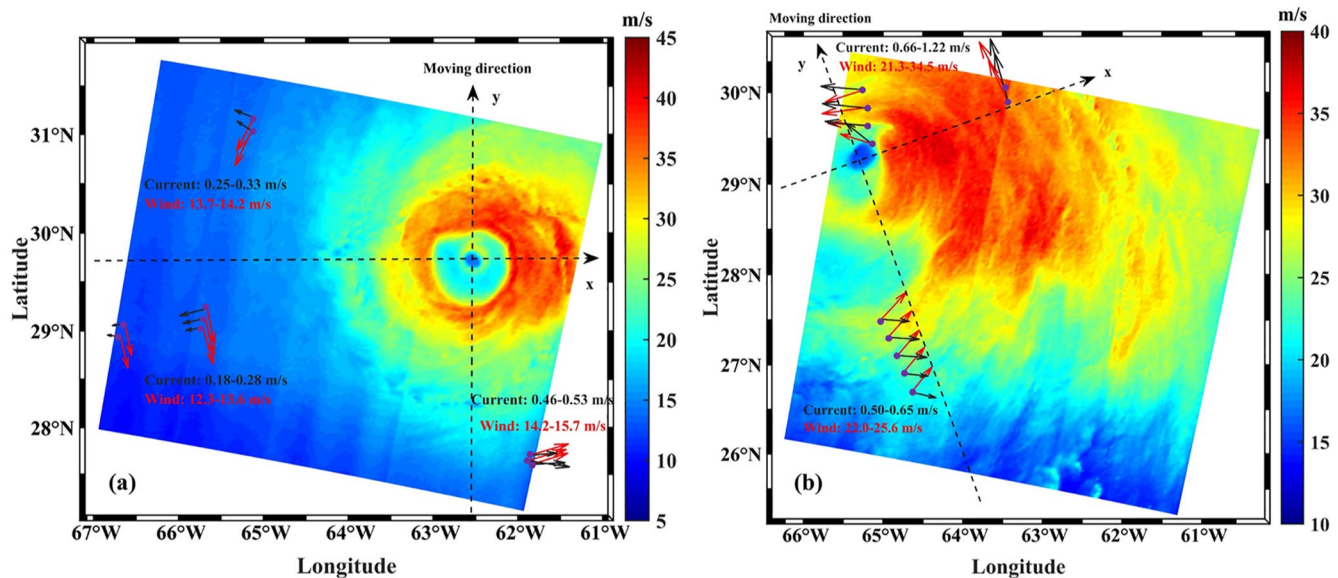


**Figure 8.** synthetic aperture radars (SAR)-derived wind fields of (a) Hurricane Bertha and (b) Hurricane Igor, using RADARSAT-2 dual-polarization imagery obtained at 10:14 UTC on 12 July 2008, and 10:11 UTC on 19 September 2010, respectively. The color bars denote the wind speed (m/s). The black and red arrows indicate the current and wind directions, respectively. The purple dots denote the locations of the drifters (the time interval between SAR wind observations and drifter current measurements is smaller than 2 hr).

the left-front and left-rear quadrants, the differences in the directions between surface winds and currents are about  $90^\circ$ , whereas the differences in the right-rear quadrant are small ( $<17^\circ$ ). In the case of Hurricane Igor, the current speeds in the right-front quadrant (0.66–1.22 m/s) are much stronger than those in the left-rear quadrant (0.50–0.65 m/s). The wind directions are approximately aligned with the current directions in the right-front quadrant. In the left-rear quadrant, the angles between the wind and current are about  $45^\circ$ . Thus, in this case, the rotations of surface winds and currents are resonant in the right-front quadrant, but this resonance is not favorable in the left-rear quadrants. These results are thus consistent with our statistical analysis in Section 3.1.

Figure 9a shows the SMAP wind field of Hurricane Kilo at 06:36 UTC on 6 September 2015. Although the spatial resolution is coarse, surface wind speed asymmetry is clearly illustrated. Wind speeds on the right side are significantly larger than those on the left side, with a maximum wind speed of 49.3 m/s. In addition to wind observations, there were six drifters located in the four quadrants of this storm, providing near-surface current measurements. The drifter-measured current speeds in the right-front quadrant (1.29–1.81 m/s) and right-rear quadrant (1.18–1.26 m/s) are higher than those in the left-front quadrant (0.34–0.55 m/s) or left-rear quadrant (0.41–0.52 m/s). This suggests that surface currents also exhibit asymmetric features. In the right-front quadrant, current directions measured by the drifters are close to, or parallel to, the hurricane-moving direction. By contrast, current directions in the left-front quadrant show significant deviations from, or are perpendicular to, the storm-moving direction. Figure 9b shows the SMOS wind field for Hurricane Igor at 08:53 UTC on 13 September 2010. For this case, the structure of the surface wind field is relatively symmetric and the maximum wind speed is 48.8 m/s. In the right-rear quadrant, the high wind speed (e.g., about 47 m/s) in the eyewall region induces a strong current (about 2 m/s). On the left side of Hurricane Igor, two drifters are in the storm periphery area and thus current speeds measured by these drifters are significantly less than those from the two drifters in the eyewall region on the right side. In the left-rear quadrant, current directions are opposite to the storm-moving direction.

#### 4. Summary

In this study, surface winds and currents are simultaneously monitored by satellite microwave sensors and drifting buoys under extreme weather conditions. A 13-year data set (2007–2020) of TC surface wind fields observed by C-band SARs (RS-2 & S1-A/B) and scatterometer (ASCAT) as well as L-band radiometers (SMAP & SMOS) were collocated with hourly current data, measured by drifters. Based on this unique data set, we analyzed the

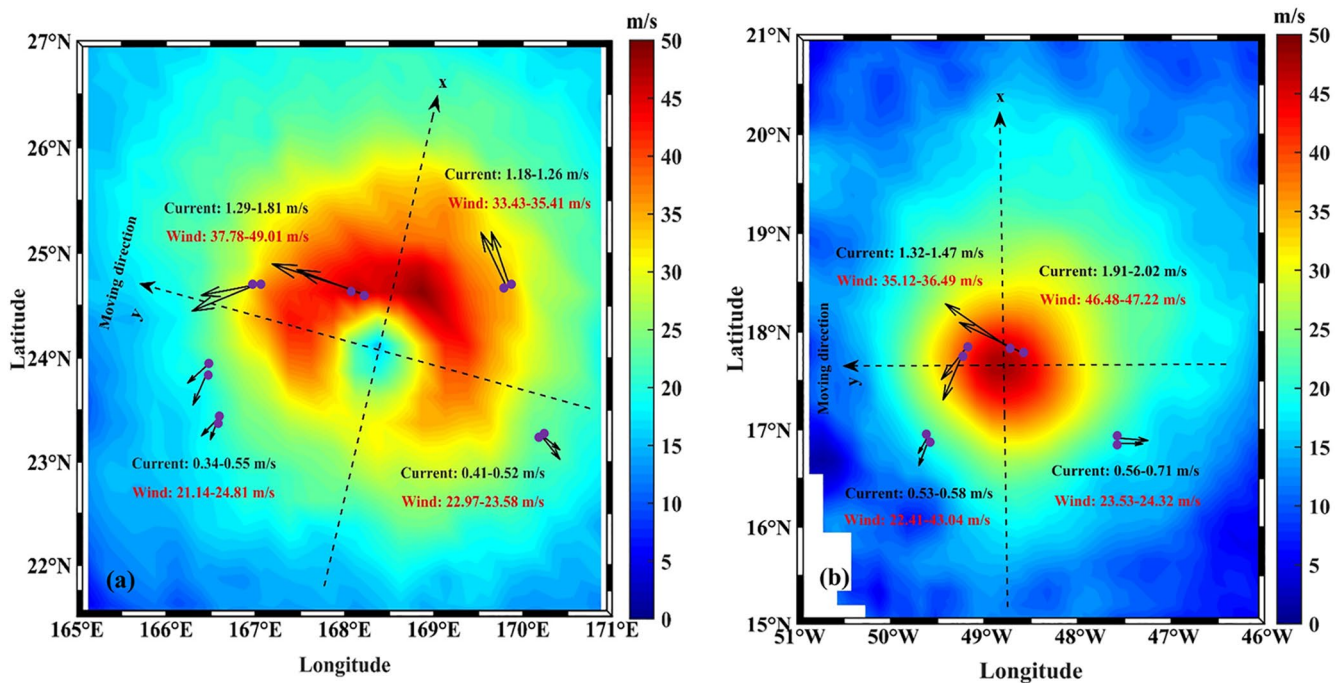


**Figure 9.** Soil Moisture Active/Passive (SMAP) wind field of (a) Hurricane Kilo at 06:36 UTC on 6 September 2015, and (b) Soil Moisture and Ocean Salinity wind field of Hurricane Igor at 08:53 UTC on 13 September 2010, respectively. The color bars denote the wind speed (m/s). The black arrows indicate the current directions. The purple dots denote the locations of the drifters (the time interval between SMAP and Soil Moisture and Ocean Salinity wind observations and drifter current measurements is smaller than 2 hr).

dependence of the ageostrophic current speed on the surface wind speed in the four TC quadrants. For high wind speeds (20–50 m/s), the near-surface ageostrophic current speeds tend to linearly increase with wind speeds, approximately, in each TC quadrant.

The near-surface mean drift ratios for the ageostrophic current were estimated and found to be different on different sides of the TC tracks. The ratios are about 2% in the left-front and left-rear quadrants and between 2% and 4% in the right-front and right-rear quadrants, respectively. The difference in the surface drift ratio is possibly related to resonance between wind stress and near-inertial currents. However, it should be pointed out that there are several other possible sources of uncertainty. Under TC conditions, heavy rainfall can attenuate the signals from SAR and scatterometer, thereby potentially biasing the wind speeds. In addition, errors in the geophysical model functions may also affect the wind speed and wind direction retrievals. Moreover, systematic errors probably exist in the drifter-measured currents, especially under high winds. Also, while baroclinic currents generated by TCs are ignored in the analysis, they are measured by drifting buoys. This is also a potential source of uncertainty because the magnitude of TC-induced baroclinic currents can be comparable to that of drifter currents. Note that satellites and drifters measure winds and currents with respect to different reference standards; the former measure winds at 10-m height above the sea surface whereas the latter at 15-m depth below the sea surface. We expect that more accurate drift ratios might be obtained if winds and currents can be observed at the same reference level (e.g., at the sea surface).

We examined surface wind and current vectors on the left and right sides of TC tracks and found that they both showed strong asymmetric characteristics. For Hurricanes Bertha and Igor, wind speeds and current speeds on the right side were significantly higher than those on the left side. The SAR-derived high-resolution wind fields clearly show that the maximum wind speeds of these two hurricanes both occur on the right side of hurricane tracks. The high wind speed of 34.5 m/s in the right-front quadrant of Hurricane Igor induced currents of 1.22 m/s in the OML. In the right-front quadrant of Hurricane Igor, wind directions were aligned with the current directions, whereas in the left-front and left-rear quadrants of Hurricane Bertha, winds and currents were almost at right angles. Therefore, the rotations of surface winds and currents are resonant on the right side, especially in

the right-front quadrant, rather than on the left side. Accurate knowledge of the asymmetry of surface winds and currents and their coupling can greatly enhance our understanding of upper ocean responses to TCs.

The asymmetry of TC surface winds and currents is also confirmed by synergistic observations from SMAP radiometer and by drifters. Although the spatial resolution of measurements from the radiometer is much lower than that of SAR, surface wind asymmetry of Hurricane Kilo is still clearly revealed. The eye of Kilo is sufficiently large that it is fully resolved by SMAP wind measurements. Compared to C-band SAR, the L-band radiometer is largely unaffected by rain and thus can provide accurate wind measurements in storms. For severe storms such as Hurricane Igor, a symmetric surface wind structure is observed by the SMOS radiometer. For this case, Igor's eye cannot be identified from the SMOS wind field, because the size of eye is smaller than the spatial resolution of the wind measurements. Moreover, it should be noted that high wind speeds (e.g., about 47 m/s) can induce strong currents (about 2 m/s) in the eyewall region.

### Data Availability Statement

RADARSAT-2 and Sentinel-1A/B SAR data can be acquired from the Earth Observation Data Management System (EODMS; <https://www.eodms-sgdot.nrcan-rncan.gc.ca>) and Distributed Active Archive Center (DAAC) of the Alaska Satellite Facility (ASF; <https://asf.alaska.edu>). ASCAT and SMAP daily gridded wind data are available at [www.remss.com](http://www.remss.com). SMOS gridded wind products are publicly available at [www.smosstorm.org](http://www.smosstorm.org). Drifter hourly current data can be obtained from [https://www.aoml.noaa.gov/phod/gdp/hourly\\_data.php](https://www.aoml.noaa.gov/phod/gdp/hourly_data.php).

### References

- Ardhuin, F., Marié, L., Rasche, N., Forget, P., & Roland, A. (2009). Observation and estimation of Lagrangian, Stokes, and Eulerian currents induced by wind and waves at the sea surface. *Journal of Physical Oceanography*, 39, 2820–2838. <https://doi.org/10.1175/2009jpo4169.1>
- Brown, J. (1991). The final voyage of Rapaiti: A measure of sea-surface drift velocity in relation to the surface wind. *Marine Pollution Bulletin*, 22, 37–40. [https://doi.org/10.1016/0025-326x\(91\)90443-v](https://doi.org/10.1016/0025-326x(91)90443-v)
- Chang, Y.-C., Chen, G.-Y., Tsen, R.-S., Centurioni, L. R., & Chu, P. C. (2012). Observed near-surface currents under high wind speeds. *Journal of Geophysical Research*, 117, C11026. <https://doi.org/10.1029/2012JC007996>
- Chang, Y.-C., Chen, G.-Y., Tsen, R.-S., Centurioni, L. R., & Chu, P. C. (2013). Observed near-surface flows under all tropical cyclone intensity level using drifter in the northwestern Pacific. *Journal of Geophysical Research: Oceans*, 118, 2367–2377. <https://doi.org/10.1002/jgrc.20187>
- Chavas, D. R., & Emanuel, K. A. (2010). A QuikSCAT climatology of tropical cyclone size. *Geophysical Research Letters*, 37, L18816. <https://doi.org/10.1029/2010GL044558>
- Chou, K.-H., Wu, C.-C., & Lin, S.-Z. (2013). Assessment of the ASCAT wind error characteristics by global dropwindsonde observations. *Journal of Geophysical Research: Atmospheres*, 118, 9011–9021. <https://doi.org/10.1002/jgrd.50724>
- Clarke, A. J., & Van Gorder, S. (2018). The relationship of near-surface flow, Stokes drift, and the wind stress. *Journal of Geophysical Research: Oceans*, 123, 4680–4692. <https://doi.org/10.1029/2018jc014102>
- Curcic, M., Chen, S. S., & Özgökmen, T. M. (2016). Hurricane-induced ocean waves and Stokes drift and their impacts on surface transport and dispersion in the Gulf of Mexico. *Geophysical Research Letters*, 43, 2773–2781. <https://doi.org/10.1002/2015gl067619>
- D'Asaro, E. A., Black, P. G., Centurioni, L. R., Chang, Y.-T., Chen, S. S., Foster, R. C., et al. (2014). Impact of typhoons on the ocean in the Pacific: ITOP. *Bulletin of the American Meteorological Society*, 95, 1405–1418.
- Edson, J. B., Jampana, V., Weller, R. A., Bigorre, S. P., Plueddemann, A. J., Fairall, C. W., et al. (2013). On the exchange of momentum over the open ocean. *Journal of Physical Oceanography*, 43, 1589–1610. <https://doi.org/10.1175/jpo-d-12-0173.1>
- Elipot, S., Lumpkin, R., Perez, R. C., Lilly, J. M., Early, J. J., & Sykulski, A. M. (2016). A global surface drifter data set at hourly resolution. *Journal of Geophysical Research: Oceans*, 121, 2937–2966. <https://doi.org/10.1002/2016jc011716>
- Fan, S., Zhang, B., Mouche, A., Perrie, W., Zhang, J. A., & Zhang, G. (2020). Estimation of wind direction in tropical cyclones using C-band dual-polarization synthetic aperture radar. *IEEE Transactions on Geoscience and Remote Sensing*, 58, 1450–1462. <https://doi.org/10.1109/tgrs.2019.2946885>
- Figa-Saldaña, J., Wilson, J. J. W., Attema, E., Gelsthorpe, R., Drinkwater, M. R., & Stoffelen, A. (2002). The advanced scatterometer (ASCAT) on the meteorological operational (MetOp) platform: A follow on for European wind scatterometers. *Canadian Journal of Remote Sensing*, 28, 404–412.
- Glenn, S. M., Miles, T. N., Seroka, G. N., Xu, Y., Forney, R. K., Yu, F., et al. (2016). Stratified coastal ocean interactions with tropical cyclones. *Nature Communications*, 7, 1–10. <https://doi.org/10.1038/ncomms10887>
- Hwang, P. A. (2011). A note on the ocean surface roughness spectrum. *Journal of Atmospheric and Oceanic Technology*, 28, 436–443. <https://doi.org/10.1175/2010jtecho812.1>
- Kudryavtsev, V., Monzikova, A., Combot, C., Chapron, B., Reul, N., & Quilfen, Y. (2019). A simplified model for the baroclinic and barotropic ocean response to moving tropical cyclones: 1. Satellite observations. *Journal of Geophysical Research: Oceans*, 124, 3446–3461. <https://doi.org/10.1029/2018jc014746>
- Liu, G., Kumar, N., Harcourt, R., & Perrie, W. (2021). Bulk, spectral and deep water approximations for Stokes drift: Implications for coupled ocean circulation and surface wave models. *Journal of Advances in Modeling Earth Systems*, 13, e2020MS002172. <https://doi.org/10.1029/2020MS002172>
- Lumpkin, R., Grodsky, S. A., Centurioni, L., Rio, M. H., Carton, J. A., & Lee, D. (2013). Removing spurious low-frequency variability in drifter velocities. *Journal of Atmospheric and Oceanic Technology*, 30, 353–360. <https://doi.org/10.1175/jtech-d-12-00139.1>
- McNally, G. J. (1981). Satellite-tracked drift buoy observations of the near-surface flow in the eastern mid-latitude North Pacific. *Journal of Geophysical Research*, 86, 8022–8030. <https://doi.org/10.1029/jc086ic09p08022>

### Acknowledgments

This work was supported in part by each of the following: the Joint Project between National Science Foundation of China and Russian Science Foundation under Grant 42061134016, the National Science Foundation under Grant 42076181, the International cooperation project of National Natural Science Foundation of China under Grant 41620104003, the Shanghai Typhoon Foundation under Grant TFIJ201902, the ESA-MOST China Dragon-5 Program under grant 58290, the Postgraduate Research & Practice Innovation Program of Jiangsu Province under grant KYCX21\_0960, the China Scholarship Council (CSC) PhD Joint Training Program under Grant 202008320521, the Government Research Initiative Program (GRIP) of the Canadian Space Agency, the Ocean Frontier Institute of Dalhousie University, and the Fisheries and Oceans Canada SWOT program.

- McWilliams, J. C., & Restrepo, J. M. (1999). The wave-driven ocean circulation. *Journal of Physical Oceanography*, 29, 2523–2540. [https://doi.org/10.1175/1520-0485\(1999\)029<2523:twdoc>2.0.co;2](https://doi.org/10.1175/1520-0485(1999)029<2523:twdoc>2.0.co;2)
- Meissner, T., Ricciardulli, L., & Wentz, F. J. (2017). Capability of the SMAP mission to measure ocean surface winds in storms. *Bulletin of the American Meteorological Society*, 98, 1660–1677. <https://doi.org/10.1175/bams-d-16-0052.1>
- Mitarai, S., & McWilliams, J. C. (2016). Wave glider observations of surface winds and currents in the core of Typhoon Danas. *Geophysical Research Letters*, 43, 11312–11319. <https://doi.org/10.1002/2016gl071115>
- Mouche, A., Chapron, B., Knaff, J., Zhao, Y., Zhang, B., & Combet, C. (2019). Copolarized and cross-polarized SAR measurements for high-resolution description of major hurricane wind structures: Application to Irma category 5 hurricane. *Journal of Geophysical Research: Oceans*, 124, 3905–3922. <https://doi.org/10.1029/2019jc015056>
- Mouche, A., Chapron, B., Zhang, B., & Husson, R. (2017). Combined co- and cross-polarized SAR measurements under extreme wind conditions. *IEEE Transactions on Geoscience and Remote Sensing*, 55, 6746–6755. <https://doi.org/10.1109/tgrs.2017.2732508>
- Peterson, R. G. (1985). Drifter trajectories through a current meter array at Drake Passage. *Journal of Geophysical Research*, 90, 4883–4893. <https://doi.org/10.1029/jc090ic03p04883>
- Price, J. F. (1981). Upper ocean response to a hurricane. *Journal of Physical Oceanography*, 11, 153–175. [https://doi.org/10.1175/1520-0485\(1981\)011<0153:uortah>2.0.co;2](https://doi.org/10.1175/1520-0485(1981)011<0153:uortah>2.0.co;2)
- Price, J. F. (1983). Internal wave wake of a moving storm. Part I: Scales, energy budget and observations. *Journal of Physical Oceanography*, 13, 949–965. [https://doi.org/10.1175/1520-0485\(1983\)013<0949:iwwoam>2.0.co;2](https://doi.org/10.1175/1520-0485(1983)013<0949:iwwoam>2.0.co;2)
- Reul, N., Chapron, B., Zabolotskikh, E., Donlon, C., Mouche, A., Tenerelli, J., et al. (2017). A new generation of tropical cyclone size measurements from space. *Bulletin of the American Meteorological Society*, 98, 2367–2385. <https://doi.org/10.1175/bams-d-15-00291.1>
- Reul, N., Chapron, B., Zabolotskikh, E., Donlon, C., Quilfen, Y., Guimard, S., & Piolle, J. F. (2016). A revised L-band radio-brightness sensitivity to extreme winds under tropical cyclones: The five year SMOS-storm database. *Remote Sensing of Environment*, 180, 274–291. <https://doi.org/10.1016/j.rse.2016.03.011>
- Reul, N., Tenerelli, J., Chapron, B., Vandemark, D., Quilfen, Y., & Kerr, Y. (2012). SMOS L-band radiometer: A new capability for Ocean Surface remote sensing in hurricanes. *Journal of Geophysical Research*, 117, C02006. <https://doi.org/10.1029/2011jc007474>
- Sanford, T. B., Price, J. F., & Girtton, J. B. (2011). Upper-ocean response to Hurricane Frances (2004) observed by profiling EM-APEX floats. *Journal of Physical Oceanography*, 41, 1041–1056. <https://doi.org/10.1175/2010jpo4313.1>
- Schyberg, H., Noer, G., Tvetter, F., & Rohrs, J. (2015). ASAR and ASCAT in polar low situations. *Journal of Atmospheric and Oceanic Technology*, 32, 783–792.
- Seroka, G., Miles, T., Xu, Y., Kohut, J., Schofield, O., & Glenn, S. (2017). Rapid shelf-wide cooling response of a stratified coastal ocean to hurricanes. *Journal of Geophysical Research: Oceans*, 122, 4845–4867. <https://doi.org/10.1002/2017jc012756>
- Shay, L. K., Martinez-Pedraja, J., Cook, T. M., Haus, B. K., & Weisberg, R. H. (2007). High-frequency radar mapping of surface currents using WERA. *Journal of Atmospheric and Oceanic Technology*, 24, 484–503. <https://doi.org/10.1175/jtech1985.1>
- Sullivan, P. P., Romero, L., McWilliams, J. C., & Melville, W. K. (2012). Transient evolution of Langmuir turbulence in ocean boundary layers driven by hurricane winds and waves. *Journal of Physical Oceanography*, 42, 1959–1980. <https://doi.org/10.1175/jpo-d-12-025.1>
- Wu, J. (1968). Laboratory studies of wind-wave interactions. *Journal of Physical Oceanography*, 13, 1441–1451. <https://doi.org/10.1017/s0022112068001783>
- Yueh, S. H., Fore, A. G., Tang, W., Hayashi, A., Stiles, B., Reul, N., et al. (2016). SMAP L-band passive microwave observations of ocean surface wind during severe storms. *IEEE Transactions on Geoscience and Remote Sensing*, 54, 7339–7350. <https://doi.org/10.1109/tgrs.2016.2600239>
- Zabolotskikh, E., Mitnik, L., & Chapron, B. (2014). GCOM-W1 AMSR2 and MetOp-A ASCAT wind speeds for the extratropical cyclones over the North Atlantic. *Remote Sensing of Environment*, 147, 89–98. <https://doi.org/10.1016/j.rse.2014.02.016>
- Zhang, B., & Perrie, W. (2012). Cross-polarized synthetic aperture radar: A new potential measurement technique for hurricanes. *Bulletin of the American Meteorological Society*, 93, 531–541. <https://doi.org/10.1175/bams-d-11-00001.1>
- Zhang, B., Perrie, W., Zhang, J. A., Uhlhorn, E. W., & He, Y. (2014). High-resolution hurricane vector winds from C-band dual-polarization SAR observations. *Journal of Atmospheric and Oceanic Technology*, 31, 272–286. <https://doi.org/10.1175/jtech-d-13-00006.1>
- Zhang, B., Zhu, Z., Perrie, W., Tang, J., & Zhang, J. A. (2021). Estimating tropical cyclone wind structure and intensity from radiometer and synthetic aperture radar. *IEEE Journal of Selected Topics in Applied Earth Observations and Remote Sensing*, 14, 4043–4050. <https://doi.org/10.1109/jstars.2021.3065866>
- Zhang, G., Perrie, W., Zhang, B., Yang, J., & He, Y. (2020). Monitoring of tropical cyclone structures in ten years of RADARSAT-2 SAR images. *Remote Sensing of Environment*, 236, 111449. <https://doi.org/10.1016/j.rse.2019.111449>
- Zhang, H., Chen, D., Zhou, L., Liu, X., Ding, T., & Zhou, B. (2016). Upper ocean response to typhoon Kalmaegi (2014). *Journal of Geophysical Research: Oceans*, 121, 6520–6535. <https://doi.org/10.1002/2016jc012064>